mater.scichina.com link.springer.com

Published online 22 September 2021 | https://doi.org/10.1007/s40843-021-1769-7
Sci China Mater 2022, 65(3): 612–619

Highly efficient $Cu_2ZnSn(S,Se)_4$ bifacial solar cell *via* a composition gradient strategy through the molecular ink

Saqib Nawaz Khan[1,2], Sijie Ge[1,2], Yuxiang Huang[1,2], Han Xu[1,2], Wentao Yang[1,2], Ruijiang Hong[3], Yaohua Mai[4], Ening Gu[1,2*], Xianzhong Lin[1,2*] and Guowei Yang[1]

ABSTRACT **The use of transparent conducting oxide (TCO) as a substrate in $Cu_2ZnSn(S,Se)_4$ (CZTSSe) thin-film solar cells allows for advanced applications, such as bifacial, semi-transparent, and tandem solar cells with the capability to increase power density generation. However, the efficiency of this kind of solar cell is still below 6% based on the low-cost solution process. In this work, we develop a composition gradient strategy and demonstrate a 6.82% efficient CZTSSe solar cell on F:SnO_2 (FTO) substrate under the ambient condition. The composition gradient is realized by simply depositing the precursor inks with different Zn/Sn ratios. To verify that the high performance of the solar cell is attributed to the composition gradient strategy rather than the sole change of the Zn/Sn ratio, devices based on absorbers with varied Zn/Sn ratios are fabricated. Furthermore, the structure and surface morphology of the CZTSSe films with/without composition gradients are examined. The presence of elemental gradient through the depth of the CZTSSe films before and after annealing is confirmed by secondary ion mass spectroscopy analysis. It is found that the composition gradient enhances the crystallinity of the absorber, reduces the surface roughness as well as device parasitic losses, contributing to a higher fill factor, open-circuit voltage, and conversion efficiency.**

Keywords: $Cu_2ZnSn(S, Se)_4$, composition gradient, bifacial solar cell, molecular ink

INTRODUCTION

Earth abundant, nontoxic kesterite $Cu_2ZnSn(S,Se)_4$ (CZTSSe) material is a promising absorber for thin-film photovoltaics. It possesses desired physical and photovoltaic properties, such as high absorption coefficient (>10^4 cm^{-1}), tunable bandgap (1.0–1.5 eV), and high theoretical conversion efficiency of 32% according to the Shockley Queisser limit [1–6]. CZTSSe solar cell has already achieved 12.6% record efficiency based on molybdenum substrate [7]. The device performance depends on several factors, including the quality of the absorber, band alignment, and back contact characteristics [8–10]. The quality of CZTSSe absorber is influenced by various parameters, including annealing condition, precursor film composition, and elemental gradient of precursor film (such as stacking order in the case of vacuum-based deposition) [11–14]. These parameters are decisive for the phase purity, defects, and band tails. In our previous work, the effects of annealing conditions were studied systematically for the devices on the transparent F:SnO_2 (FTO) substrate, which suggests the combination of high temperature, short time, and higher amount of chalcogen through a rapid thermal annealing process is crucial to get high-quality film as well as preserve a good back interface characteristic [15]. Besides, using different elemental compositions, the performance of CZTSSe devices on Mo substrate has been investigated, suggesting that Zn rich, Cu, and Sn poor composition is beneficial to suppressing the formation of deep level defects [16–20]. However, Zn rich and Cu, Sn poor composition leads to B-type defect clusters, such as $2Zn_{Cu}$, Zn_{Sn}, and Zn(S,Se) secondary phases in the CZTSSe film [18]. In this case, although Zn self-regulates at the surface, an excessive amount of Zn diffuses to the bottom [16]. Studies on the metallic stacking order show that a large amount of Zn near the back contact in precursor film diffuses to the surface, generating voids in the resultant film [12,21]. In contrast to non-stoichiometric higher Zn/Sn composition, stoichiometric or lower Zn/Sn composition leads to A-type detrimental deep-level defect clusters, such as Cu_{Zn}, Sn_{Zn} deep-level defects, and Cu_x(S,Se) and CuSn(S,Se) secondary phases [18].

On the other hand, Sn is more volatile and evaporates in the form of SnS from the surface during the annealing [22,23]. This volatility of Sn from the surface could produce Sn deficiency at the surface, which leads to Sn gradient and would result in Sn diffusion from the bottom to the top of film during the annealing process. This shows that due to the unlike nature of CZTSSe metal species, the unbalanced molecular interdiffusion process during the annealing could result in thin films with different elemental compositions in bulk, surface, and back contact. The other factor is the unfavorable band alignment of CZTSSe/CdS heterojunction, which leads to the non-radiative recombination in the space charge region [24,25]. It is found that Zn rich at the surface of CZTSSe results in the formation of $Cd_{1-x}Zn_xS$ by Zn and Cd inter-diffusion at the junction, consequently reducing the conduction band offset [12,21,26]. Based

[1] Guangzhou Key Laboratory of Flexible Electronic Materials and Wearable Devices, State Key Laboratory of Optoelectronic Materials and Technologies, School of Materials Science and Engineering, Sun Yat-Sen University, Guangzhou 510275, China
[2] Key Laboratory of Polymeric Composite and Functional Materials of Ministry of Education, Sun Yat-Sen University, Guangzhou 510275, China
[3] School of Physics, Sun Yat-Sen University, Guangzhou 510275, China
[4] Institute of New Energy Technology, College of Information and Technology, Jinan University, Guangzhou 510632, China
* Corresponding authors (emails: guen@mail.sysu.edu.cn (Gu E); linxzh8@mail.sysu.edu.cn (Lin X))

on the above-ascribed analysis, it is reasonable to use a lower amount of Zn at the bottom and a higher amount of Zn at the top to facilitate the molecular inter-diffusion during the annealing process.

Some efforts have been dedicated to kesterite-based bifacial solar cells, but the efficiency is still lower compared with the conventional Mo-based solar cells [27–37]. The high parasitic loss was reported to be one of the reasons when using transparent conducting oxide (TCO) as a back contact [29–36], although a slightly higher efficiency of 7.9% was achieved by using a vacuum-based process combined with a complex interlayer modification of the back interface [37]. Apart from that, deposition of 10 nm Ge layer on the top of sputtered precursor film, MgF_2 anti-reflective coating, and long annealing time (over 60 min) have been applied to make the result possible. On the other hand, when using a solution-based approach, only 5.8% efficient CZTSSe solar cell was obtained on indium-tin-oxide (ITO)-coated glass [31].

In this work, the concept of the elemental gradient is adopted to vary the elemental concentration of precursor film throughout the thickness. This gradient strategy can help to control the properties of CZTSSe film in the bulk, surface as well as near the back contact. We varied Zn/Sn composition gradients in the precursor film to scrutinize its effect on the resulting CZTSSe thin film and corresponding device performance and compared the results with samples prepared from inks with different Zn/Sn ratios. By employing Zn/Sn composition gradient, the quality of CZTSSe/CdS heterojunction improves, and the parasitic losses are reduced significantly, contributing to a higher fill factor (FF). Furthermore, the reduction of Zn concentration at the bottom of the film decreases the chances of ZnS segregation near the back contact. Consequently, the total area conversion efficiency of the device based on a gradient Zn/Sn composition improves significantly from 5.56% to 6.82% in comparison with that of the sample prepared with a single Zn/Sn ratio.

EXPERIMENTAL SECTION

CZTSSe thin film and device fabrication

Copper(II) chloride (analytical grade (AR), 98%), zinc acetate (AR, 99.5%), tin(II) chloride dihydrate (AR, 99.99%), thiourea (AR, 99%), selenium powder (AR, 99.9%), sodium chloride (AR, 99.99%), and *N*,*N*-dimethylformamide (DMF) (99.5%) were purchased from Shanghai Macklin biochemical co. Ltd. Tin(II) sulfide (AR, 99.5%) and dimethyl-sulfoxide (DMSO) (AR, >99%) were purchased from Alfa Aesar and Aladin biochemical technology co. Ltd., respectively. All chemicals were used directly without further purification.

The precursor ink was prepared by dissolving copper(II) chloride (1.65 mmol), tin chloride dihydrate (1 mmol), zinc acetate (1.5 mmol), sodium chloride (0.2075 mmol), and thiourea (5.395 mmol) in a mixed solvent consisting of DMF (1.2 mL) and DMSO (1.8 mL) under magnetic stirring at room temperature. A transparent solution with light yellow color was obtained and filtered with a 450-nm filter before spin coating.

FTO-coated glass with a total thickness of 2.2 mm and a sheet resistance of 7 Ω/square was subsequentially cleaned with acetone, ethanol, and deionized water for 15 min at 50°C, followed by plasma treatment. The CZTS precursor solution was spin-coated on the cleaned FTO substrate at 2000 r min^{-1} for 50 s, then 4000 r min^{-1} for 10 s, followed by pre-annealing at 320°C for 2 min. The spin coating and pre-annealing steps were repeated several times to obtain precursor films with a desired thickness.

Rapid thermal processing was applied to prepare the absorber. The as-deposited CZTSSe precursor film was placed in a graphite box containing 500 mg selenium powder and about 6 mg SnS powder. The samples were heated from room temperature to 540°C in 20 s and then kept at 540°C for 7 min. Before starting the annealing process, the quartz tube furnace was evacuated to remove moisture and impurities. Then N_2 gas was used to fill the furnace until the pressure reached ambient pressure. These processes were repeated three times. The device was completed by sequentially depositing the CdS buffer layer, intrinsic zinc oxide (i: ZnO) and tin-doped indium oxide (In_2O_3:Sn) layers, and final Ag electrode, as discussed elsewhere [38]. Devices with a total area of 0.36 cm^2 were separated by mechanical scribing. Additionally, no antireflection coating was applied.

Powder X-ray diffraction (XRD, MiniFlex Rikagu) using Cu Kα radiation and Raman spectroscopy (Renishaw inVia reflex spectrometer) with an excitation wavelength of 633 nm were used to characterize the microstructure of the film. Field-emission scanning electron microscopy (COXEM, Kurashiki Kako, 20 kV) and atomic force microscopy (Bruker Icon Dimension AFM) were used to characterize the film morphology. The composition depth profiles were obtained by secondary ion mass spectroscopy (ION TOF-SIMS 5), and a 30 keV Bi cluster primary ion gun was used for this analysis, along with O_2^+ ion guns for sputtering. The performance of the solar cell was measured using an AM 1.5 solar simulator (Enlitech, SS-5F-3A) with an illumination intensity of 100 mW cm^{-2} (1 sun) calibrated by Si reference solar cell (Enlitech). The external quantum efficiency (EQE) spectrum was obtained with an Enlitech QE-R setup calibrated by Si and Ge reference (OSI optoelectronics).

RESULTS AND DISCUSSION

The XRD patterns of CZTSSe films prepared with different Zn/Sn ratios and gradient compositions (see Table 1) on FTO are shown in Fig. 1. Major peaks observed at 2-theta of 27.22°–27.33°, 45.26°–45.43° and 53.56°–53.80° can be assigned to (112), (200/204), and (312/116) planes of kesterite CZTSSe (CZTSe (JCPDS 53-0868) and CZTS (JCPDS 26-0575)). Furthermore, peaks corresponding to FTO substrate are also detected and marked with the # symbol in Fig. 1a. No other peaks related to impurities and secondary phases are observed. The Scherrer [39], Williamson, and Smallman equations [40] are used to estimate the average grain size D, microstrain ε, and dislocation density σ, respectively, in CZTSSe films based on the major peak of (112) for all the samples.

$$D = k\lambda / \beta\cos\theta, \quad (1)$$

$$\varepsilon = \beta\cos\theta / 4, \quad (2)$$

$$\sigma = 1 / D^2, \quad (3)$$

where D is the average crystallite size perpendicular to reflecting plane, k is the shape factor constant ranging from 0.8 to 1.2 (typically equal to 0.9), λ is the incident X-ray wavelength, β is the full width at half maximum (FWHM) of the peak, and θ is the Braggs angle in radian.

The calculated value of D is plotted as a function of the Zn/Sn ratio and gradient composition in Fig. 1b. The average grain size increases from 25.95 to 40.47 nm, with an increasing Zn/Sn ratio

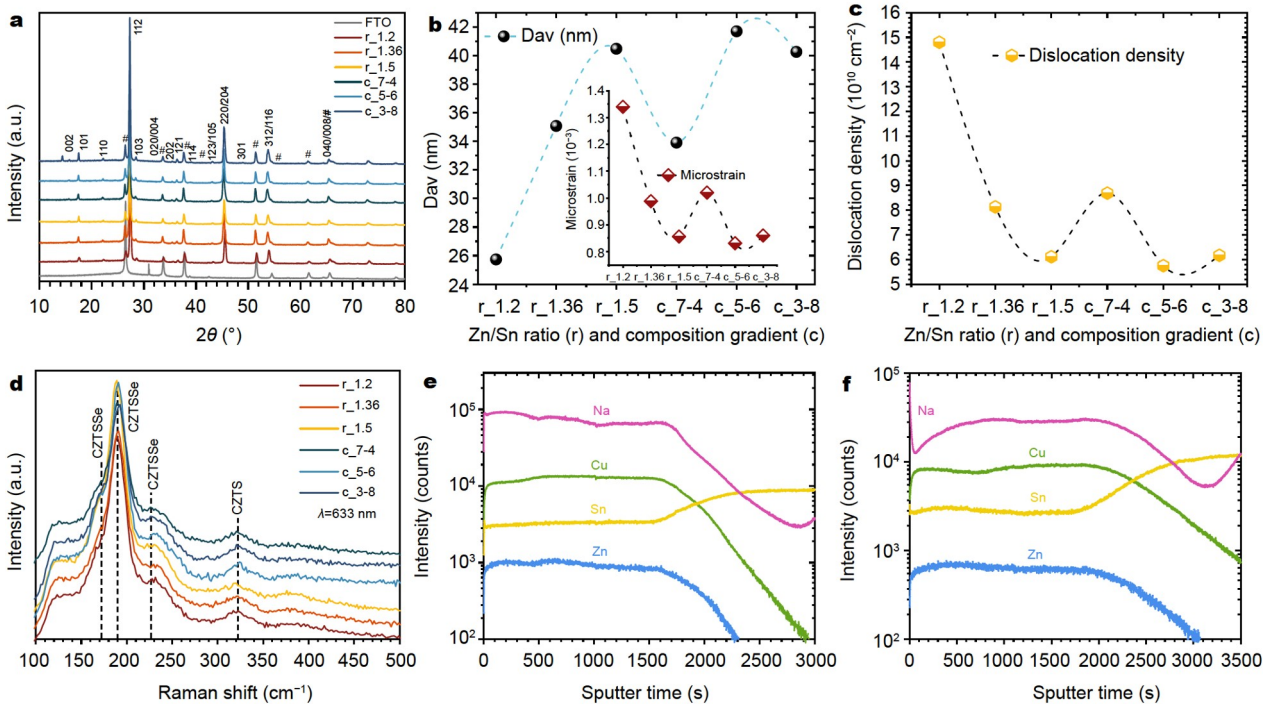

Figure 1 (a) XRD patterns, (b) average crystallite size and microstrain evolution (inset), (c) the dislocation density, (d) recorded Raman spectra with an excitation wavelength of 633 nm. Elemental depth profile using TOF-SIMS of (e) CZTSSe precursor film, and (f) sample c_5-6, an annealed CZTSSe absorber, which delivers the device with the best performance.

from 1.2 to 1.5. Compared with single Zn/Sn = 1.2 sample, the composition gradient sample c_7-4 prepared with (Zn/Sn = 1.2)-dominant using a combination of 7 layers Zn/Sn = 1.2 at the bottom and 4 layers Zn/Sn = 1.5 on the top shows a better crystalline quality and has an average crystallite size of 33.91 nm. By increasing Zn content at the top with 6 layers Zn/Sn = 1.5 and 5 layers Zn/Sn = 1.2 at the bottom, the average crystallite size is further improved to 41.70 nm. However, the average crystallite size decreases to 40.27 nm when further increasing Zn content in the precursor film by using the combination of 8 layers Zn/Sn = 1.5, 3 layers Zn/Sn = 1.2, at the top and bottom, respectively (c_3-8), showing a reverse tendency towards single Zn/Sn = 1.5 sample. Based on the above-mentioned analysis, we can conclude that the improvement in average crystallite size is due to the composition gradient in precursor film rather than the sole increase of Zn/Sn ratio.

The inset of Fig. 1b shows the effect of different Zn/Sn ratios and composition gradients on the reduction of microstrain and dislocation density for the corresponding CZTSSe thin film. The microstrain ε, reduces from 1.34×10^{-3} to 0.85×10^{-3} with the increasing Zn/Sn ratio from 1.2 to 1.5, which further declines to 0.83×10^{-3} by employing composition gradient (sample c_5-6). Furthermore, the dislocation density σ, is reduced apparently from 14.8×10^{10} to 6.11×10^{10} lines cm^{-2} when the Zn/Sn ratio increases from 1.2 to 1.5, which further drops to 5.75×10^{10} lines cm^{-2} by employing Zn/Sn composition gradient with a combination of 5 layers Zn/Sn = 1.2 and 6 layers Zn/Sn = 1.5 (sample c_5-6), as shown in Fig. 1c.

The XRD patterns of some secondary phases, such as Zn(S,Se), $Cu_2Sn(S,Se)_3$ (cubic structure) [41], and $Cu_3Sn(S,Se)_4$ (tetragonal structure) [42], overlap with CZTSSe and they cannot be distinguished by XRD. Raman spectroscopy was used to further analyze the phase purity of CZTSSe sample. It should be noted that the recorded Raman spectra only give the characteristics of the top surface layer of CZTSSe film, which is about 170 nm when an excitation wavelength of 633 nm is used [43]. A dominant peak in the range of 189.15–192.68 cm^{-1} and a shoulder at 171.44–174.0 cm^{-1} in all the samples are detected, which correspond to the A mode of CZTSSe, while the shoulders at 222–226 cm^{-1}, 232–234 cm^{-1}, and 240–243 cm^{-1} (223, 233, 243 cm^{-1}) correspond to E mode of kesterite CZTSSe [44–46]. The intensity of the shoulder at about 170 cm^{-1} can be assigned to two A symmetry and two B symmetry modes. A mode corresponds to vibration of Se, while B mode attributes to Cu/Zn and Cu/Sn atomic planes' vibration. The intensity of B mode is lower for all the samples, which indicates a copper-poorer composition. This could result in copper vacancy (V_{Cu}) and consequently prevents the formation of Cu_{Zn} anti-site disorder [47].

Fig. 1e shows the elemental distribution depth profile of CZTSSe precursor film prepared with 6 layers Zn/Sn = 1.5 and 5 layers Zn/Sn = 1.2 at the top and bottom, respectively, to create Zn/Sn composition gradient. The depth profile of the precursor film shows that the signal intensity count for Zn is lower at the bottom but higher at the top, which agrees well with the precursor ink deposition pattern. Fig. 1f shows the depth profile of sample 'c_5-6' after annealing; lower intensity counts for Zn signal at the bottom is observed, which is in agreement with the precursor film. The lower amount of Zn near the back would be helpful to avoid the formation of ZnS(Se) secondary phase near the back contact, which leads to high series resistance in the device, deteriorating the device performance [16]. It should be noted that the amount of Sn is kept constant while Zn is varied in precursor inks. The intensity counts of Sn show a slight

decline at the top of precursor film, which may either be attributed to Sn evaporation during the pre-annealing or the diffusion of Sn towards the back contact.

After annealing, in contrary to the precursor film, the intensity counts of Sn increase at the top, indicating that Sn diffuses from the bottom to the top of CZTSSe film. The other possible reason of comparatively higher intensity of Sn near the surface could be related to the incorporation of Sn, provided by the SnS used during the annealing process. The depth profile of the Cu signal shows a decline in intensity at the top of precursor film, which reduces after annealing, as shown in Fig. 1f. We speculate that a lower amount of Cu in precursor film would assist the formation of the CuSe liquid phase in the bulk rather at the surface of CZTSSe thin film during the annealing process. Accordingly, it results in a uniform grain growth throughout the film.

Fig. 2a shows the top-view scanning electron microscopy (SEM) images of all the CZTSSe samples after selenization. Small and dense grains can be observed with cracks on the surface of CZTSSe film prepared with the Zn/Sn = 1.2 ink. The samples prepared with inks of lower Zn/Sn ratios show cracks after annealing, which are mentioned as r_1.2 and r_1.36. With increasing Zn/Sn ratio from 1.2 to 1.5, the surface morphology is improved, as grain shape changes from round tips to larger grains with sharp edges and random orientations. The sample prepared with Zn/Sn composition gradient with a combination of 5 layers Zn/Sn = 1.2 and 6 layers of Zn/Sn = 1.5 (c_5-6) shows a similar surface morphology to the Zn/Sn = 1.5 sample (r_1.5).

AFM was used to further investigate the surface morphology of CZTSSe films prepared with different Zn/Sn ratios and composition gradients, as shown in Fig. 2b, c. the CZTSSe film of sample 'r_1.2' consists of small grains and low surface roughness with an average root mean square (RMS) value of 58.53 nm. The grain height increases with the increase of Zn/Sn ratio to 1.5, which indicates a larger vertical dimension of CZTSSe film grains, while the surface roughness decreases as the average RMS value is reduced from 58.53 to 40.12 nm. The sample prepared with Zn/Sn composition gradient with a combination of 5 layer 1.2 and 6 layer of 1.5 also shows large grains with a reduced average RMS value of 29.82 nm. The reduction of surface roughness is beneficial for the subsequent CdS deposition, enabling better coverage and better junction quality.

Device characterization

Fig. 3a and Table 1 show current-voltage (*J*-*V*) characteristics and corresponding cell parameters of all the CZTSSe devices under the front illumination, respectively. The power conversion efficiency (PCE) increases from 3.89% to 5.56% with an

Table 1 List of samples prepared with different Zn/Sn ratios from 1.2 to 1.5, represented as r_1.2, r_1.36, r_1.5; samples with gradient compositions of Zn/Sn = 1.2 at the bottom, Zn/Sn = 1.5 at the top are represented as c_7-4, c_5-6, and c_3-8.

Sample name	Zn/Sn = 1.2	Zn/Sn = 1.36	Zn/Sn = 1.5
r_1.2	11 layers	–	–
r_1.36	–	11 layers	–
r_1.5	–	–	11 layers
c_7-4	7 layers (bottom)	–	4 layers (top)
c_5-6	5 layers (bottom)	–	6 layers (top)
c_3-8	3 layers (bottom)	–	8 layers (top)

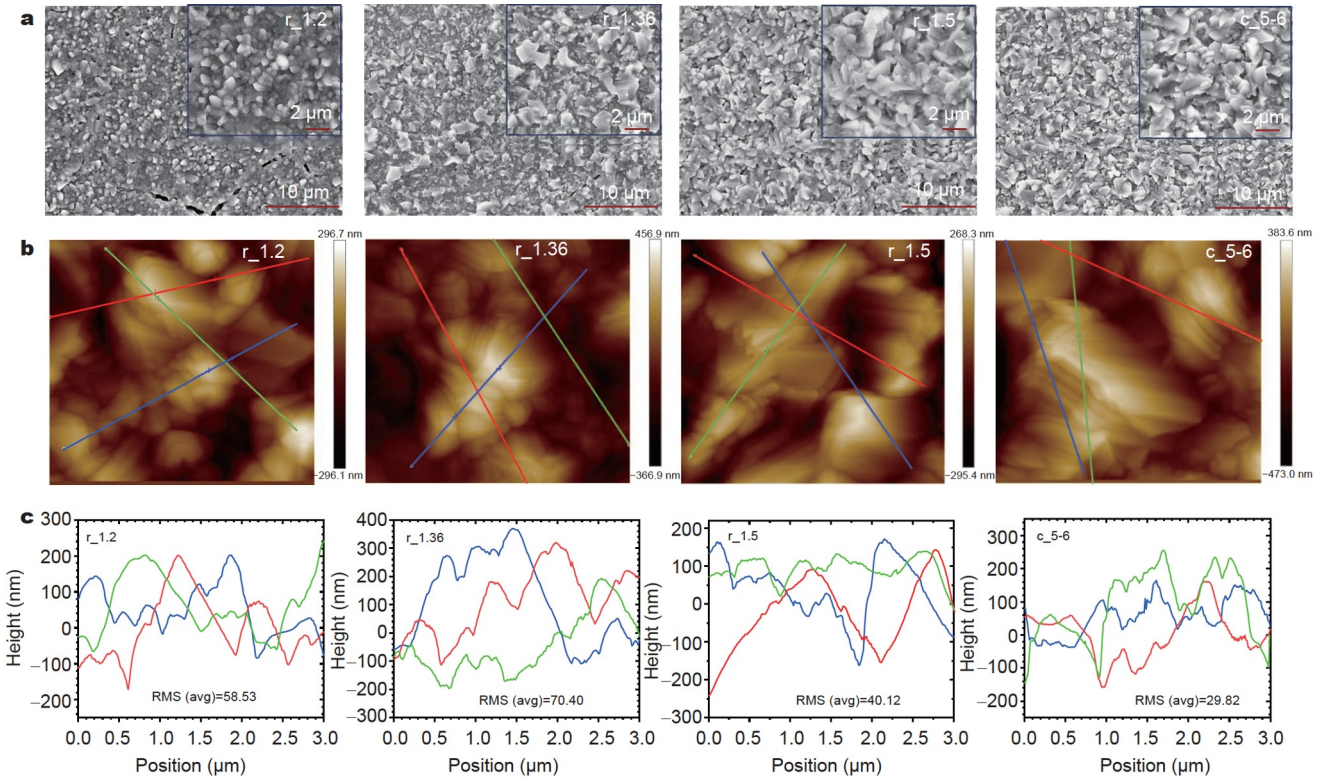

Figure 2 (a) Top view of SEM images, (b) AFM surface topography images, and (c) corresponding height profiles of CZTSSe absorber films prepared with different Zn/Sn ratios and gradients.

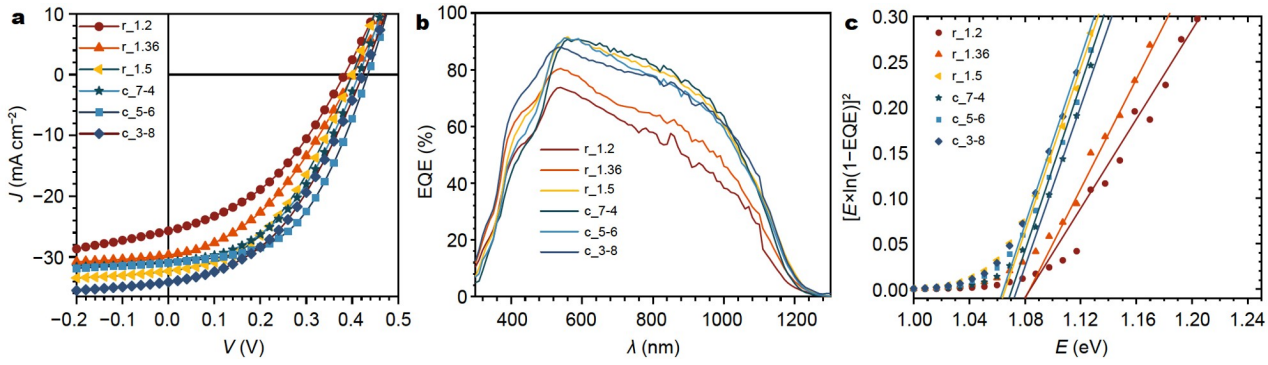

Figure 3 (a) *J-V* curves, (b) EQE curves of the typical bifacial solar cells under one Sun (AM 1.5 G) front illumination, prepared with different Zn/Sn ratios from 1.2 to 1.5 and composition gradients, and (c) corresponding bandgap values extracted from $[E \times \ln(1 - \mathrm{EQE})]^2$ *versus* energy ($h\nu$) plot.

increasing Zn/Sn ratio from 1.2 to 1.5, showing a similar evolution trend with our previous study based on the Mo substrate [16]. The higher Zn content in precursor film (over Zn/Sn = 1.5) results in segregation of Zn near the back contact and at grain boundaries as well as an increased surface roughness, which deteriorates the device performance. By using Zn/Sn composition gradient with a high Zn content (Zn/Sn = 1.5) at the top and low Zn content (Zn/Sn = 1.2) at the bottom (c_7-4), a better PCE of 5.75% is achieved. Similarly, by further increasing the Zn content on the top and reducing it at the bottom (sample c_5-6), the PCE is dramatically enhanced from 5.75% to 6.82%. However, further increase of Zn amount in the precursor film (with Zn/Sn = 1.5 dominant) reduces the device performance to 6.20%, showing a tendency back towards sample made with single Zn/Sn = 1.5. The trend agrees well with the average crystalline quality decrement obtained from XRD analysis.

These results demonstrate the effectiveness of using gradient strategy to improve the device performance. Assuming the thickness of each layer is constant, the overall composition of sample c_5-6 should be similar to that of sample r_1.36 prepared with single Zn/Sn = 1.36. However, the PCE of sample r_1.36 is 2% in absolute lower than that of the sample c_5-6, which further verifies that the enhancement of the device performance originates from the composition gradient in precursor film, rather than the change of composition.

The statistic distribution of cells' parameters as a function of different Zn/Sn ratios and gradients are shown in Fig. 4. As the Zn/Sn ratio increases from 1.2 to 1.5, the overall performance of solar cells improves. Open-circuit voltage (V_{OC}), FF, and short-circuit current density (J_{SC}) show a similar trend as the Zn/Sn ratio increases. The V_{OC} profile of the device prepared with Zn/Sn = 1.2 is more scattered than that of all the other samples, which can be attributed to cracks, as confirmed by SEM analysis. Compared with the single Zn/Sn = 1.2 sample, the composition gradient sample prepared with Zn/Sn = 1.2 dominant (i.e., c_7-4) shows improvement in overall device performance. By increasing Zn content at the top and reducing it at the bottom (c_5-6), the overall PCE is enhanced, due to the significant improvement in FF and V_{OC}. However, further increasing the Zn content at the top in the gradient precursor film, the overall device performance drops again (c_3-8). The overall improvement in device performance compared with all samples prepared with a single Zn/Sn ratio ink could be associated with a smoother surface, allowing a better deposition of CdS.

EQE curve, as shown in Fig. 3b, gives the photo conversion response of the CZTSSe thin-film devices, prepared with different Zn/Sn ratios and Zn/Sn composition gradients. EQE increases with the increasing Zn/Sn ratio from 1.2 to 1.5, while there is no significant change for all the samples prepared with Zn/Sn gradient. The J_{SC} value extracted from EQE is given in Table 2, which is slightly lower than that obtained from *J-V* measurement for Zn/Sn 1.2, 1.36 samples. This may be attributed to the surface roughness and difference in the active area during the *J-V* and EQE characterizations. The samples prepared with Zn/Sn = 1.5 and gradients exhibit better EQE response and give J_{SC} values in the range of 32.7 to 33.1 mA cm^{-2}. The optical band gap is obtained by plotting $[E \times \ln(1 - \mathrm{EQE})]^2$ *versus* incident photon energy E, and estimated to be in the range of 1.06 to 1.08 eV for all the samples [48].

The shunt conduction G_{sh}, series resistance R_s and ideality factor A are important factors for achieving high conversion efficiency, which can be obtained from the single exponential diode equation [49–51].

$$J = J_0 \exp\left[\frac{q}{AKT}(V - R_s J)\right] + G_{sh} V - J_L, \tag{4}$$

$$r(J) = \frac{\mathrm{d}V}{\mathrm{d}J} = R_s + \frac{AKT}{q}(J + J_L)^{-1}, \tag{5}$$

where J_0 is the reverse saturation current density. K is Boltzmann constant, and q is the elementary charge on the electron. Fig. 5 shows the plots of dV/dJ *versus* $(J + J_{SC})^{-1}$, and dJ/dV *versus* V. Shunt conduction is the measure of current flowing through an alternative path in the photovoltaic absorber. Low crystalline quality results in small grains and increasing grain boundaries. Grain boundaries could act as shunting paths for electron and holes when there are deep defects at the grain boundaries. In this case, the increase of grain boundaries reduces the photo-generated current by providing an alternative path. From XRD and SEM analysis, we can observe that with increasing Zn/Sn ratio from 1.2 to 1.5, the crystalline quality of CZTSSe film improves, which leads to larger crystallite size and hence reduces the grain boundaries. Consequently, a dramatic drop in shunt conduction is observed from 16.3 to 2.4 mS cm^{-2} with the increasing Zn/Sn ratio from 1.2 to 1.5, reaching the minimum in sample c_7-4 (Table 3). The ideality factor drops from 4.4 to 1.7 as the Zn/Sn ratio increases from 1.2 to 1.5, which is in the range of 1.7–2.2 when using a composition gradient strategy (Table 3).The series resistance first increases with increasing Zn/Sn ratio and then decreases with Zn/Sn gradient. The PCE increases from 3.89% to 5.56% by first increasing Zn/Sn ratio from 1.2 to 1.5 and then

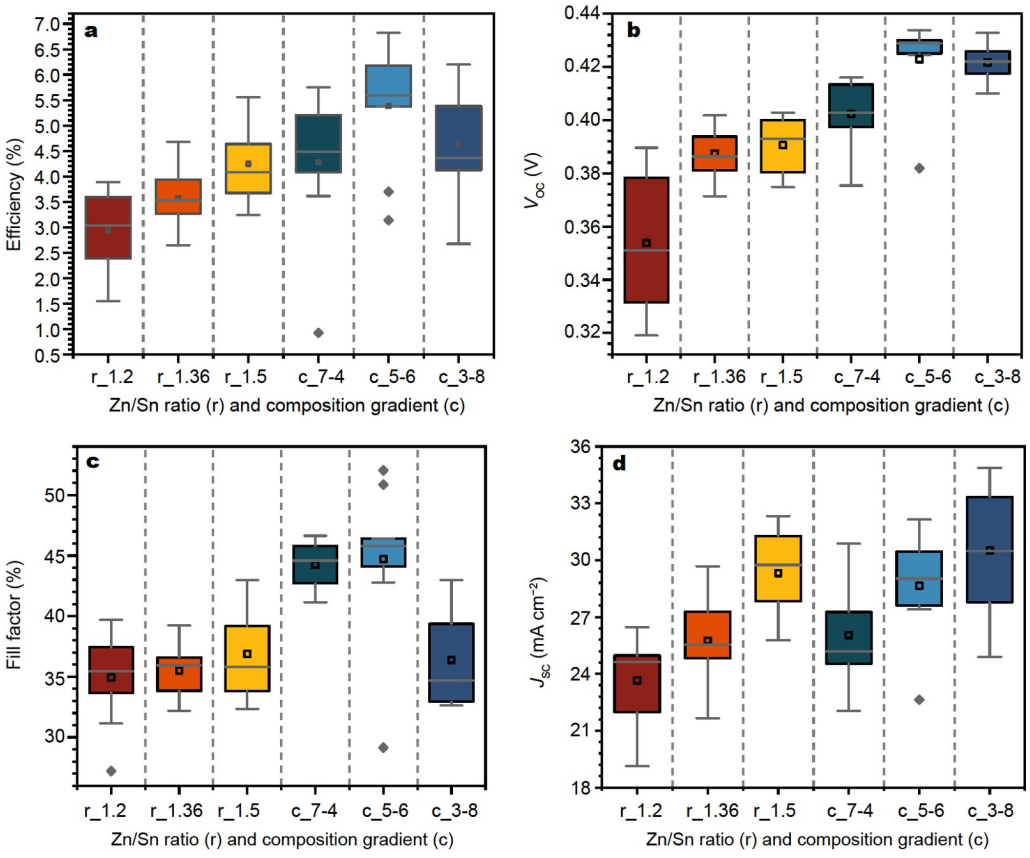

Figure 4 Statistics of device parameters of samples prepared with different Zn/Sn ratios from 1.2 to 1.5 and Zn/Sn composition gradient: (a) efficiency, (b) open-circuit voltage (V_{OC}), (c) FF, and (d) short-circuit current density (J_{SC}).

Table 2 Detailed device parameters of all samples. The bandgap is extracted from the Tauc plot.

Zn/Sn	PCE (%)	V_{OC} (V)	FF (%)	J_{SC} (mA cm^{-2}) (*J-V*)	Band gap (eV)	J_{SC} derived from EQE (mA cm^{-2})
r_1.2	3.89	0.383	39.5	25.7	1.08	24.7
r_1.36	4.67	0.401	39.2	29.7	1.06	27.8
r_1.5	5.56	0.400	43.0	32.3	1.08	33.1
c_7-4	5.75	0.414	45.0	30.9	1.06	32.7
c_5-6	6.82	0.433	50.9	30.9	1.06	32.3
c_3-8	6.20	0.423	43.0	34.1	1.08	32.9

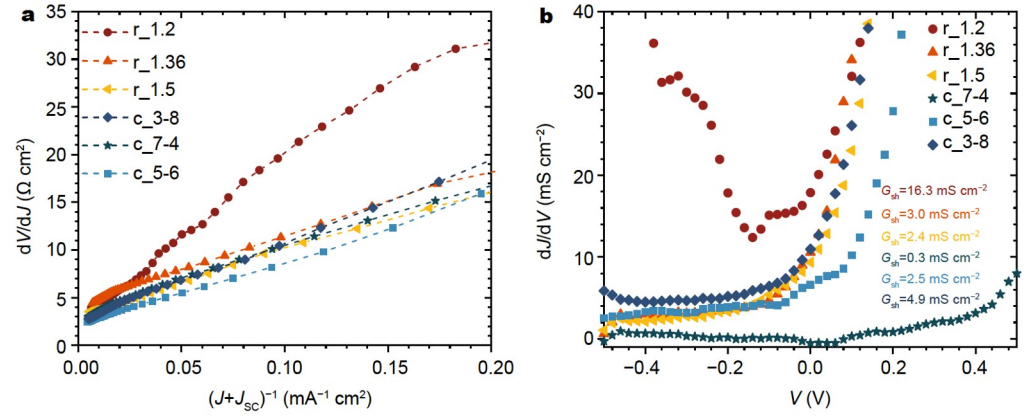

Figure 5 (a) Plots of dV/dJ *versus* $(J + J_{SC})^{-1}$ used to determine series resistance R, and ideality factor A. (b) Plots of dJ/dV *versus* V used to determine the shunt conduction G_{sh} for CZTSSe thin-film solar cells prepared with different Zn/Sn ratios and gradient extracted from *J-V* characteristics under AM 1.5 front illumination of corresponding cells.

Table 3 G_{sh}, R_s and A of CZTSSe thin-film devices prepared with different Zn/Sn ratios and gradients under AM 1.5G illumination

Sample	G_{sh} (mS cm^{-2})	R_s (Ω cm)	A
r_1.2	16.3	2.6	4.4
r_1.36	3.0	4.2	1.9
r_1.5	2.4	3.1	1.7
c_7-4	0.3	3.1	1.8
c_5-6	2.5	2.2	1.7
c_3-8	4.9	2.5	2.2

reach 6.82% by employing Zn/Sn ratio due to the reduced parasitic losses and the improvement of ideality factor. The overall lower parasitic losses and better ideality factor of sample c_5-6 prepared with a combination of 5 layers Zn/S = 1.2 and 6 layers of Zn/Sn = 1.5 composition gradient lead to higher V_{OC}, FF, and hence higher device performance.

CONCLUSIONS

In summary, we report the fabrication of highly efficient CZTSSe solar cell on FTO substrate using a composition gradient strategy. The composition gradient in the precursor film is realized by varying the number of coating layers from each ink with different Zn/Sn ratios. By tailoring the composition gradient condition, CZTSSe films with larger average crystalline size, lower microstrain, and less dislocation are achieved. Furthermore, using a gradient is beneficial for the improvement of the surface morphology, with the surface roughness RMS decreasing to 29.82 nm. The total area PCE of the device is raised from 3.89% to 5.56% with the increasing of Zn/Sn ratio from 1.2 to 1.5, while using a composition gradient strategy enables a significant improvement of the PCE to 6.82% under the front illumination due to the reduction of parasitic losses and enhancement of CZTSSe/CdS junction quality. This is the record efficiency of CZTSSe solar cells on TCO substrate based on solution processing. This work provides a facile composition gradient strategy for CZTSSe absorbers to achieve high-efficiency thin-film solar cells.

Received 12 July 2021; accepted 9 August 2021; published online 22 September 2021

1 Katagiri H, Jimbo K, Maw WS, *et al.* Development of CZTS-based thin film solar cells. Thin Solid Films, 2009, 517: 2455–2460
2 Mitzi DB, Gunawan O, Todorov TK, *et al.* The path towards a high-performance solution-processed kesterite solar cell. Sol Energy Mater Sol Cells, 2011, 95: 1421–1436
3 Ki W, Hillhouse HW. Earth-abundant element photovoltaics directly from soluble precursors with high yield using a non-toxic solvent. Adv Energy Mater, 2011, 1: 732–735
4 Ramasamy K, Malik MA, O'Brien P. Routes to copper zinc tin sulfide Cu_2ZnSnS_4 a potential material for solar cells. Chem Commun, 2012, 48: 5703–5714
5 Wang D, Zhao W, Zhang Y, *et al.* Path towards high-efficient kesterite solar cells. J Energy Chem, 2018, 27: 1040–1053
6 Shockley W, Queisser HJ. Detailed balance limit of efficiency of p-n junction solar cells. J Appl Phys, 1961, 32: 510–519
7 Wang W, Winkler MT, Gunawan O, *et al.* Device characteristics of CZTSSe thin-film solar cells with 12.6% efficiency. Adv Energy Mater, 2014, 4: 1301465
8 Crovetto A, Hansen O. What is the band alignment of $Cu_2ZnSn(S,Se)_4$ solar cells? Sol Energy Mater Sol Cells, 2017, 169: 177–194
9 Sardashti K, Chagarov E, Antunez PD, *et al.* Nanoscale characterization of back surfaces and interfaces in thin-film kesterite solar cells. ACS Appl Mater Interfaces, 2017, 9: 17024–17033
10 Wang D, Wu J, Guo H, *et al.* Tuning the work function of the metal back contact toward efficient $Cu_2ZnSnSe_4$ solar cells. Sol RRL, 2021, 5: 2000391
11 Zhao Y, Han X, Chang L, *et al.* Effects of selenization conditions on microstructure evolution in solution processed $Cu_2ZnSn(S,Se)_4$ solar cells. Sol Energy Mater Sol Cells, 2019, 195: 274–279
12 Liu X, Guo J, Hao R, *et al.* Cliff-like conduction band offset at CdS/Cu_2ZnSnS_4 heterojunction prepared by sputtering CuSn alloy target using different stacking order. Sol Energy, 2019, 183: 285–292
13 Shin SW, Pawar SM, Park CY, *et al.* Studies on Cu_2ZnSnS_4 (CZTS) absorber layer using different stacking orders in precursor thin films. Sol Energy Mater Sol Cells, 2011, 95: 3202–3206
14 Olgar MA, Klaer J, Mainz R, *et al.* Effect of precursor stacking order and sulfurization temperature on compositional homogeneity of CZTS thin films. Thin Solid Films, 2016, 615: 402–408
15 Khan SN, Ge SJ, Gu EN, et al. Bifacial $Cu_2ZnSn(S,Se)_4$ thin film solar cell based on molecular ink and rapid thermal processing. Adv Mater Interfaces, 2021, doi: 10.1002/admi.202100971.
16 Ge S, Xu H, Huang Y, *et al.* Surprising efficiency enhancement of $Cu_2ZnSn(S,Se)_4$ solar cells with abnormal Zn/Sn ratios. Sol RRL, 2020, 4: 2000325
17 Li S, Lloyd MA, McCandless BE, *et al.* Effects of cation composition on carrier dynamics and photovoltaic performance in $Cu_2ZnSnSe_4$ monocrystal solar cells. Sol Energy Mater Sol Cells, 2020, 205: 110255
18 Chen S, Wang LW, Walsh A, *et al.* Abundance of Cu_{Zn} + Sn_{Zn} and 2Cu_{Zn} + Sn_{Zn} defect clusters in kesterite solar cells. Appl Phys Lett, 2012, 101: 223901
19 Duan B, Shi J, Li D, *et al.* Underlying mechanism of the efficiency loss in CZTSSe solar cells: Disorder and deep defects. Sci China Mater, 2020, 63: 2371–2396
20 Sun Y, Qiu P, Wang S, *et al.* Defect control for high-efficiency $Cu_2ZnSn(S,Se)_4$ solar cells by atomic layer deposition of Al_2O_3 on precursor film. Sol RRL, 2021, 5: 2100181
21 Zhang S, Hadi HD, Wang Y, *et al.* A precursor stacking strategy to boost open-circuit voltage of Cu_2ZnSnS_4 thin-film solar cells. IEEE J Photovoltaics, 2018, 8: 856–863
22 Weber A, Mainz R, Schock HW. On the Sn loss from thin films of the material system Cu-Zn-Sn-S in high vacuum. J Appl Phys, 2010, 107: 013516
23 Scragg JJ, Ericson T, Kubart T, *et al.* Chemical insights into the instability of Cu_2ZnSnS_4 films during annealing. Chem Mater, 2011, 23: 4625–4633
24 Yan C, Huang J, Sun K, *et al.* Cu_2ZnSnS_4 solar cells with over 10% power conversion efficiency enabled by heterojunction heat treatment. Nat Energy, 2018, 3: 764–772
25 Wang S, Shen Z, Wu J, *et al.* Nanoscale surface electrical properties tailored by room-temperature sulfurization for high-efficient CZTSe solar cells. Adv Mater Interfaces, 2020, 7: 2000564
26 Wang S, Shen Z, Sun Y, *et al.* Defects and surface electrical property transformation induced by elemental interdiffusion at the p-n heterojunction *via* high-temperature annealing. ACS Appl Mater Interfaces, 2021, 13: 12211–12220
27 Sarswat PK, Free ML. Demonstration of a sol-gel synthesized bifacial CZTS photoelectrochemical cell. Phys Status Solidi A, 2011, 208: 2861–2864
28 Ge J, Chu J, Jiang J, *et al.* Characteristics of in-substituted CZTS thin film and bifacial solar cell. ACS Appl Mater Interfaces, 2014, 6: 21118–21130
29 Ge J, Chu J, Jiang J, *et al.* The interfacial reaction at ITO back contact in kesterite CZTSSe bifacial solar cells. ACS Sustain Chem Eng, 2015, 3: 3043–3052
30 Ge J, Chu J, Yan Y, *et al.* Co-electroplated kesterite bifacial thin-film solar cells: A study of sulfurization temperature. ACS Appl Mater Interfaces, 2015, 7: 10414–10428
31 Ge J, Yu Y, Ke W, *et al.* Improved performance of electroplated CZTS thin-film solar cells with bifacial configuration. ChemSusChem, 2016,

9: 2149–2158
32 Kim JS, Kang JK, Hwang DK. High efficiency bifacial $Cu_2ZnSnSe_4$ thin-film solar cells on transparent conducting oxide glass substrates. APL Mater, 2016, 4: 096101
33 Espindola-Rodriguez M, Sylla D, Sánchez Y, *et al.* Bifacial kesterite solar cells on FTO substrates. ACS Sustain Chem Eng, 2017, 5: 11516–11524
34 Wang Z, Tao J, Xiao W, *et al.* Influence of deposition potential on Cu_2ZnSnS_4 thin-film solar cells co-electrodeposited on fluorine-doped tin oxide substrates. J Alloys Compd, 2017, 701: 465–473
35 Franckevičius M, Pakštas V, Grincienė G, *et al.* Efficiency improvement of superstrate CZTSSe solar cells processed by spray pyrolysis approach. Sol Energy, 2019, 185: 283–289
36 Kim JS, Kim DH, Hwang DK. Efficiency enhancement of bifacial $Cu_2ZnSnSe_4$ thin-film solar cells on indium tin oxide glass substrates by suppressing In-Sn diffusion with Mo interlayer. J Power Sources, 2018, 400: 9–15
37 Becerril-Romero I, Sylla D, Placidi M, *et al.* Transition-metal oxides for kesterite solar cells developed on transparent substrates. ACS Appl Mater Interfaces, 2020, 12: 33656–33669
38 Ge S, Gao H, Hong R, *et al.* Improvement of $Cu_2ZnSn(S,Se)_4$ solar cells by adding *N*,*N*-dimethylformamide to the dimethyl sulfoxide-based precursor ink. ChemSusChem, 2019, 12: 1692–1699
39 Patterson AL. The scherrer formula for X-ray particle size determination. Phys Rev, 1939, 56: 978–982
40 Williamson GK, Smallman RE. III. Dislocation densities in some annealed and cold-worked metals from measurements on the X-ray Debye-Scherrer spectrum. Philos Mag, 1956, 1: 34–46
41 Riha SC, Parkinson BA, Prieto AL. Solution-based synthesis and characterization of Cu_2ZnSnS_4 nanocrystals. J Am Chem Soc, 2009, 131: 12054–12055
42 Fernandes PA, Salomé PMP, Cunha AF. A study of ternary Cu_2SnS_3 and Cu_3SnS_4 thin films prepared by sulfurizing stacked metal precursors. J Phys D-Appl Phys, 2010, 43: 215403
43 Fernandes PA, Salomé PMP, da Cunha AF. Study of polycrystalline Cu_2ZnSnS_4 films by raman scattering. J Alloys Compd, 2011, 509: 7600–7606
44 Salomé PMP, Fernandes PA, da Cunha AF. Morphological and structural characterization of $Cu_2ZnSnSe_4$ thin films grown by selenization of elemental precursor layers. Thin Solid Films, 2009, 517: 2531–2534
45 Fernandes PA, Salomé PMP, da Cunha AF. Growth and Raman scattering characterization of Cu_2ZnSnS_4 thin films. Thin Solid Films, 2009, 517: 2519–2523
46 Grossberg M, Krustok J, Raudoja J, *et al.* Photoluminescence and Raman study of $Cu_2ZnSn(Se_xS_{1-x})_4$ monograins for photovoltaic applications. Thin Solid Films, 2011, 519: 7403–7406
47 Dimitrievska M, Fairbrother A, Saucedo E, *et al.* Influence of compositionally induced defects on the vibrational properties of device grade $Cu_2ZnSnSe_4$ absorbers for kesterite based solar cells. Appl Phys Lett, 2015, 106: 073903
48 Wang S, Jiang Z, Shen Z, *et al.* Promising Cd-free double buffer layer in CZTSSe thin film solar cells. Sci China Mater, 2021, 64: 288–295
49 Hegedus SS, Shafarman WN. Thin-film solar cells: Device measurements and analysis. Prog Photovolt-Res Appl, 2004, 12: 155–176
50 Swartz GA. Computer model of amorphous silicon solar cell. J Appl Phys, 1982, 53: 712–719
51 Sites JR, Mauk PH. Diode quality factor determination for thin-film solar cells. Sol Cells, 1989, 27: 411–417

Acknowledgements This work was supported by the National Natural Science Foundation of China (62074168), and the Fundamental Research Foundations for the Central Universities (20lgpy04). We also thank Prof. Hui Shen, Prof. Wan Yue, Prof. Zhengke Li and Prof. Zhuang Xie for the facility support.

Author contributions Lin X conceived and supervised the project; Khan SN conducted most of the experiments and wrote the draft of the manuscript; Ge S and Huang Y prepared some of the samples. Xu H supported the annealing of samples. Yang W performed X-ray diffraction measurements; Hong R, Mai Y and Yang G participated in the discussion and analysis of the data. Khan SN, Gu E and Lin X wrote the manuscript with discussion and input from all the authors.

Conflict of interest The authors declare that they have no conflict of interest.

Saqib Nawaz Khan received his Master's degree in materials physics and chemistry from Sun Yat-Sen University in 2021. Currently he is pursuing his doctoral degree at the Institute of Physics, Chinese Academy of Sciences. His research interest includes the synthesis and characterization of energy materials and their applications in optoelectronic devices. His current research focus is on kesterite $Cu_2ZnSn(S,Se)_4$ and perovskite thin-film solar cells.

Ening Gu received her PhD degree in materials science from Friedrich-Alexander-Universität Erlangen-Nürnberg in 2019 under the supervison of Prof. Christoph J. Brabec. Currently, she works as a postdoctoral fellow at the School of Materials Science and Engineering, Sun Yat-Sen University. Her research interests focus on emerging photovoltaic materials, solution-processed optoelectronic semiconductors and devices.

Xianzhong Lin received his PhD degree from Technische Universität Berlin, Germany, in 2014. Before joining Sun Yat-Sen University as an associate professor in 2017, he worked as a postdoctoral researcher at Helmholtz-Zentrum Berlin für Materialien und Energie and Friedrich-Alexander-Universität Erlangen-Nürnberg for three years. His research focuses on highly efficient and stable thin-film solar cells based on printing approach.

基于成分梯度策略制备高效率铜锌锡硫硒双面电池

Saqib Nawaz Khan[1,2], 葛思洁[1,2], 黄宇翔[1,2], 徐菡[1,2], 杨文韬[1,2], 洪瑞江[3], 麦耀华[4], 顾鄂宁[1,2*], 林显忠[1,2*], 杨国伟[1]

摘要 使用透明导电氧化物玻璃作为铜锌锡硫硒(CZTSSe)薄膜太阳电池的衬底可拓展其应用范围, 如双面电池、半透明电池或者叠层电池. 目前, 基于溶液法制备的该类太阳电池的光电转换效率仍低于6%. 本文中, 我们开发了一种成分梯度策略, 并在空气环境中于掺氟二氧化锡衬底上制备出了光电转换效率为6.82%的CZTSSe薄膜太阳电池. 成分梯度主要是通过沉积具有不同Zn/Sn比的分子前驱体溶液来实现的. 为了证明电池性能的提高归因于成分梯度, 而非单纯改变Zn/Sn比, 本工作制备并比较了基于不同Zn/Sn比吸收层的器件性能. 此外, 本工作对有/无成分梯度的CZTSSe薄膜的结构和表面形貌进行了研究, 并通过二次离子质谱分析证实了退火前后CZTSSe薄膜成分的深度梯度分布. 研究发现, 成分梯度策略改善了吸收层的结晶性, 降低了吸收层的表面粗糙度及器件的寄生损耗, 从而提高了填充因子、开路电压和转换效率.

